PHYSICAL REVIEW MATERIALS **6**, 025401 (2022)

First-principles simulations of Li boracites $Li_4B_7O_{12}Cl$ and $Li_5B_7O_{12.5}Cl$

Yan Li and N. A. W. Holzwarth
Department of Physics, Wake Forest University, Winston-Salem, North Carolina 27109, USA

(Received 27 November 2021; accepted 13 January 2022; published 7 February 2022)

Lithium boracite crystals have been identified as promising ion conductors for possible use in all-solid-state batteries. With the help of first-principles modeling techniques, we are able to show that these materials have structures with natural interstitial sites which play important roles in Li ion migration processes. The arrangements of these natural interstitial sites follow from group theory analyses of the computed and experimentally analyzed structures. Specifically, the low-temperature α phase of $Li_4B_7O_{12}Cl$ is computed to have the face-centered rhombohedral $R3c$ structure which is closely related to an ideal face-centered cubic $F\bar{4}3c$ structure with 24 natural interstitial sites per conventional unit cell. Li ion diffusion in this material is found to proceed largely by a concerted motion involving these interstitial sites and two neighboring host lattice sites, consistent with the large measured ionic conductivity of this material. Adding one addition Li_2O cluster per formula unit to $Li_4B_7O_{12}Cl$ forms $Li_5B_7O_{12.5}Cl$, which crystallizes in the face-centered cubic $F23$ structure, a subgroup of the $F\bar{4}3c$ structure. While these $F23$ crystals have 16 natural interstitial sites per conventional unit cell, their distribution is such that they do not participate in Li ion diffusion mechanisms, as is consistent with the negligible ionic conductivity measured for this material. Phonon spectral analyses of $Li_4B_7O_{12}Cl$ in its $R3c$ structure and $Li_5B_7O_{12.5}Cl$ in its $F23$ structure show that both crystals are dynamically stable. Chemical stability of these materials is indicated by convex hull analysis of $Li_4B_7O_{12}Cl$ and $Li_5B_7O_{12.5}Cl$ with respect to their building blocks of LiCl, Li_2O, and B_2O_3.

DOI: 10.1103/PhysRevMaterials.6.025401

I. INTRODUCTION

Recent literature has identified lithium boracites as promising ion-conducting electrolytes for possible use in all-solid-state batteries. These materials are related to the naturally occurring magnesium borate mineral, $Mg_3B_7O_{13}Cl$, which is characterized by a rigid framework of B-O bonds composed of triangular BO_3 and tetrahedral BO_4 units, together with a regular void structure. The magnesium borate mineral has been found in several crystalline forms including a face-centered cubic structure ($F\bar{4}3c$; space group [1] no. 219) determined in 1973 from a single crystal specimen by Sueno and coworkers [2].

Lithium boracite was developed and characterized in the 1970s by a number of authors including Levasseur and coworkers [3–6] and Jeitschko and coworkers [7,8]. This work established that $Li_4B_7O_{12}Cl$ has the same borate framework and void structure of the boracite minerals and showed that the Li ions are associated with the void channels of the structure which serve to facilitate their mobility. More recent work [9–12] has developed efficient synthesis methods. For example, using the so-called low-temperature ionothermal synthesis method, Tan and coworkers [12] were able to improve the degree of purity of samples of $Li_4B_7O_{12}Cl$, resulting in the enhancement of the Li ion mobilities with measured room-temperature ionic conductivity up to 3×10^{-4} S/cm. Their work also found that $Li_4B_7O_{12}Cl$ presents a wide voltage stability window and, more generally, exhibits promising performance with Li metal electrodes. Other recent work has studied improved ionic conductivity due to alloying on the halogen site [8,13] and on the boron site [14,15]. On the other hand, the addition of Li_2O to $Li_4B_7O_{12}Cl$ with the end composition of $Li_5B_7O_{12.5}Cl$ was studied by several authors [6,16,17] who showed that the additional Li_2O systematically reduces the ionic conductivity by several orders of magnitude. Extrapolating the measured ionic conductivity data [6] to room temperature estimates the room-temperature conductivity of $Li_5B_7O_{12.5}Cl$ to be smaller than 10^{-10} S/cm.

In order to improve the promising electrolyte properties of lithium boracites, it is useful to examine the detailed crystal structures and to study mechanisms of ionic conductivity. With the help of first-principles modeling techniques, we are able to show that lithium boracites are beautiful examples of structures with natural interstitial sites which play important roles in Li ion migration processes. In this case, the natural interstitial structure follows from group theory analysis of the ideal ground-state structure and related structures.

This paper focuses on a detailed comparison of the lithium boracites $Li_4B_7O_{12}Cl$ and $Li_5B_7O_{12.5}Cl$. The general calculation methods are briefly described in Sec. II. Section III presents the results of the optimized structures of the idealized crystals, including identifying the optimized structure of α-$Li_4B_7O_{12}Cl$ and showing how it is related to the ideal cubic $F\bar{4}3c$ structure and a plausible model for β-$Li_4B_7O_{12}Cl$. The optimization of the $Li_5B_7O_{12.5}Cl$ structure and comparison with the α-$Li_4B_7O_{12}Cl$ structure help explain the decrease in ionic conductivity, following the work of Vlasse and coworkers [16]. The phonon analyses of the ground-state structures of $Li_4B_7O_{12}Cl$ and $Li_5B_7O_{12.5}Cl$ show that both structures are dynamically stable as discussed in Sec. IV. In Sec. V, we examined the relative stability of the two materials with respect to their possible decompositions. Section VI examines the Li ion migration mechanisms for the supercells of bulk materials using both trajectory analysis and molecular dynamics simulations. The molecular dynamics results approximately follow experimental conductivity measurements. The results of this study are discussed and summarized in Sec. VII.

II. COMPUTATIONAL METHODS

The computational methods were based on density functional theory (DFT) [18,19] and density functional perturbation theory (DFPT) [20–24], using the projector augmented wave (PAW) [25] formalism. The modified generalized gradient formulation known as PBEsol [26] was used to treat the exchange and correlation effects. The PAW basis and projector functions for Li, B, O, and Cl were generated by the ATMOPAW code [27]. Simulations for the primitive and conventional models of the studied crystals were carried out using ABINT [28,29] and QUANTUM ESPRESSO packages [30,31]. To be specific, the lattice optimization and phonon calculations based on primitive unit cells were performed using ABINIT package with plane-wave expansions of the wave functions including $|\mathbf{k}+\mathbf{G}|^2 \leqslant 70\,\text{Bohr}^{-2}$ and with a $\mathbf{k}$-point sampling of $4 \times 4 \times 4$ to approximate the Brillouin zone integrals. The phonon modes were evaluated with $|\mathbf{k}+\mathbf{G}|^2 \leqslant 50\,\text{Bohr}^{-2}$ on a regular $4 \times 4 \times 4$ grid of $\mathbf{q}$ vectors in the irreducible Brillouin zone of each crystal. Investigations of Li ions migration were evaluated by using the QUANTUM ESPRESSO package, using eight-formula unit conventional cells for both $Li_4B_7O_{12}Cl$ and $Li_5B_7O_{12.5}Cl$. For these large systems, the Brillouin zone integrals could be well approximated by sampling the single $\mathbf{k} = 0$ point. To achieve well-converged wave functions, the plane-wave expansions were chosen to be $|\mathbf{k}+\mathbf{G}|^2 \leqslant 64\,\text{Bohr}^{-2}$. Structural visualizations were constructed using the XCRYSDEN [32] and VESTA [33] software packages. The program FINDSYM [34] was used in analyzing symmetry properties of the optimized crystal structures.

III. CRYSTAL STRUCTURES

A. $Li_4B_7O_{12}Cl$

In 1977, Jeitschko and coworkers [8] carried out single-crystal analyses of the crystalline phases of $Li_4B_7O_{12}Cl$, finding three distinct phases, designated as α, β, and γ. The high-temperature γ phase, stable at temperature $T > 348$ K, is fully characterized with the face-centered cubic space group [1] $F\bar{4}3c$ (no. 219) with temperature-dependent partial occupancies of Li sites. The β phase is stable within the temperature range $348\,\text{K} > T > 310\,\text{K}$ while the α phase is stable at temperatures below 310 K. From the discontinuities of the ionic conductivity plots at the transition temperatures, one expects that latent heat is associated with each of these transitions, consistent with the first-order transition designation. Jeitschko and coworkers [8] provided some information on the structures of the β and α phases, but the detailed analysis was not possible at the time. It was suggested that the α structure has a rhombohedrally distorted lattice with space group $R3$ (no. 146) with lattice constant $a = 12.141$ Å and rhombohedral angle $\alpha = 90.083$ deg. The β structure was suggested to have the cubic space group symmetry of $P\bar{4}3n$ (no. 218) with lattice constant $a = 12.161$ Å. Additionally, Jeitschko and coworkers [8] were able to perform a constrained analysis of the x-ray patterns of the α and β phases by assuming the face-centered cubic structure $F\bar{4}3c$. This scheme finds differing Li ion occupancies on the sites, as labeled by their conventional cell multiplicities and Wyckoff letters, 24c and 32e. While these correlations provide guidance to the structural analysis, they do not tell the full story of the low-temperature structures. A visualization of the $F\bar{4}3c$ structure based on the analysis of Ref. [8] is shown in Fig. 1. This visualization presents the geometry of the B_7O_{12} framework in terms of connected BO_4 tetrahedra and BO_3 planar triangles. It is interesting to note that while all of the O ion sites are geometrically equivalent corresponding to the multiplicity and Wyckoff letter 96h, there are two types of B ion sites. The tetrahedral B ion sites correspond to the label 24d while the triangular B ion sites correspond to 32e. These triangular B ion sites are geometrically and symmetrically related to fractionally occupied Li ion sites having the same 32e label.

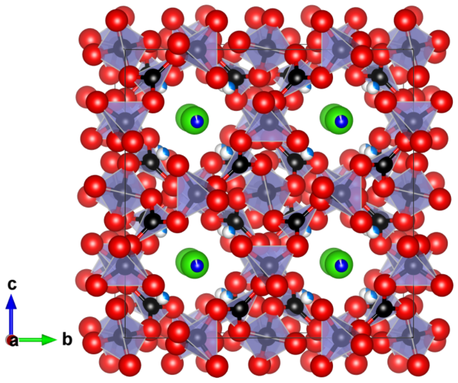

FIG. 1. Ball and stick diagram of conventional cell of $Li_4B_7O_{12}Cl$ in the $F\bar{4}3c$ structure as analyzed from single-crystal samples at room temperature [8]. Ball colors of blue, black, red, and green indicate Li, B, O, and Cl ions, respectively. The polyhedral constructions illustrate the BO_4 tetrahedra and BO_3 planar triangular structures. The dark blue balls indicate Li ions at the fully occupied 24c sites, while the partially filled light blue balls indicate Li ions at the 25% occupied 32e sites.

Using computation, we are in a position to examine the likely ground-state structure, the α structure, which has not yet been analyzed from the experiment data. Starting from the available data [8] of the ideal $F\bar{4}3c$ model and assuming 1/4th occupancy of the 32e sites, we systematically computed the total energies of the 28 unique configurations of the primitive cell. Figure 2 shows the relative static lattice energy per formula unit for each optimized atomic arrangement with an index ranging from no. 1 to 28. The results indicate that all the relaxed configurations are energetically divided into three distinct groups. While both high-energy groups are found to have the space group $P1$, the four lowest energy configurations, nos. 3, 11, 15, and 28, are identified as having rhombohedral lattice with space group $R3c$ (no. 161).

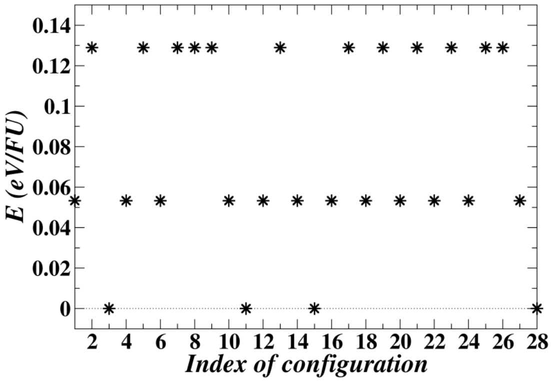

FIG. 2. The relative static lattice energy per formula unit for the 28 optimized configurations of $Li_4B_7O_{12}Cl$ in the primitive lattice setting.

Those four symmetrically equivalent structures are ordered with fully occupied Li sites. From these results, it seems likely that the ideal ground-state form of α-$Li_4B_7O_{12}Cl$ is characterized by the $R3c$ space group in a face-centered structure. This result is similar but not identical to the single-crystal analysis of Jeitschko and coworkers [8]. Specifically, the $R3c$ structure differs from the $R3$ structure suggested by the experimental work [8] by having three additional symmetry operations.

Rhombohedral structures appear to be the least commonly realized structures in nature. Interestingly, for a face-centered structure with the $R3c$ space group, the $R3c$ space group symmetry applies to both the primitive and conventional cell structures. Generally, a rhombohedral crystal has three lattice vectors of equal length and equal angles between each pair of lattice vectors. For the conventional unit cell setting, we denote the lattice vector length as a_c and the angle between lattice vectors as θ_c. The cubic structure is a special case with $\theta_c = 90$ deg. More generally, a convenient representation of the conventional lattice vectors of a rhombohedral structure similar to that used in the QUANTUM ESPRESSO code [30,31] is given by

$$\begin{aligned}
\mathbf{a_c} &= a_c(\hat{\mathbf{x}}(\lambda_c + 2\mu_c) + \hat{\mathbf{y}}(\lambda_c - \mu_c) + \hat{\mathbf{z}}(\lambda_c - \mu_c)),\\
\mathbf{b_c} &= a_c(\hat{\mathbf{x}}(\lambda_c - \mu_c) + \hat{\mathbf{y}}(\lambda_c + 2\mu_c) + \hat{\mathbf{z}}(\lambda_c - \mu_c)),\\
\mathbf{c_c} &= a_c(\hat{\mathbf{x}}(\lambda_c - \mu_c) + \hat{\mathbf{y}}(\lambda_c - \mu_c) + \hat{\mathbf{z}}(\lambda_c + 2\mu_c)).
\end{aligned} \tag{1}$$

Here

$$\lambda_c \equiv \frac{\sqrt{1 + 2\cos\theta_c}}{3} \quad \text{and} \quad \mu_c \equiv \frac{\sqrt{1 - \cos\theta_c}}{3}. \tag{2}$$

The primitive cell for our face-centered rhombohedral lattice is given by

$$\begin{aligned}
\mathbf{a_p} &= \tfrac{1}{2}(\mathbf{a_c} + \mathbf{b_c})\\
&= a_p(\hat{\mathbf{x}}(\lambda_p + \mu_p) + \hat{\mathbf{y}}(\lambda_p + \mu_p) + \hat{\mathbf{z}}(\lambda_p - 2\mu_p)),\\
\mathbf{b_p} &= \tfrac{1}{2}(\mathbf{b_c} + \mathbf{c_c})\\
&= a_p(\hat{\mathbf{x}}(\lambda_p - 2\mu_p) + \hat{\mathbf{y}}(\lambda_p + \mu_p) + \hat{\mathbf{z}}(\lambda_p + \mu_p)),\\
\mathbf{c_p} &= \tfrac{1}{2}(\mathbf{a_c} + \mathbf{c_c})\\
&= a_p(\hat{\mathbf{x}}(\lambda_p + \mu_p) + \hat{\mathbf{y}}(\lambda_p - 2\mu_p) + \hat{\mathbf{z}}(\lambda_p + \mu_p)),
\end{aligned} \tag{3}$$

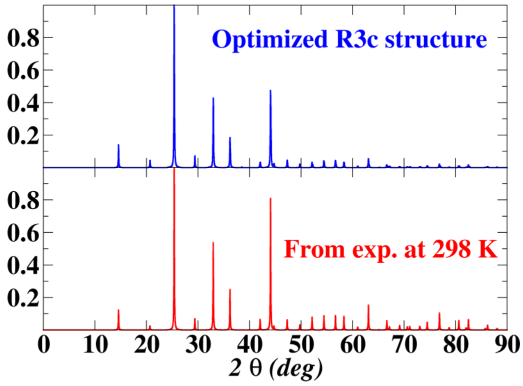

FIG. 3. X-ray patterns determined from structural analysis of $Li_4B_7O_{12}Cl$ for wavelength $\lambda = 1.54056$ Å as calculated using MERCURY software [35] from the computed idealized $R3c$ structure (top) and the analysis of single-crystal data at 298 K based on the $F\bar{4}3c$ space group reported by Jeitschko and coworkers [8].

Here

$$\lambda_p \equiv \frac{\sqrt{1 + 2\cos\theta_p}}{3} \quad \text{and} \quad \mu_p \equiv \frac{\sqrt{1 - \cos\theta_p}}{3}, \tag{4}$$

and the primitive cell length is

$$a_p = \frac{a_c}{\sqrt{3 - 2\cos(\theta_p)}}. \tag{5}$$

The relationship of the primitive angle and the conventional angle is given by

$$\cos(\theta_p) = \frac{1 + 3\cos(\theta_c)}{2[1 + \cos(\theta_c)]} \quad \text{or} \quad \cos(\theta_c) = \frac{2\cos(\theta_p) - 1}{3 - 2\cos(\theta_p)}, \tag{6}$$

where the special case of face-centered cubic corresponds to $\theta_p = 60$ deg. Note that the volume of primitive cell, V_p, is

$$V_p = a_p^3[1 - \cos(\theta_p)]\sqrt{1 + 2\cos(\theta_p)}, \tag{7}$$

which is 1/4th the volume of the conventional cell, as expected.

The atomic positions $\mathbf{R}^a$ within the unit cell can be expressed in terms of the fractional coordinates of the conventional cell (x_c, y_c, z_c) or the fractional coordinates of the primitive cell (x_p, y_p, z_p), with the relationship between the two being

$$\begin{aligned}
x_p &= x_c + y_c - z_c,\\
y_p &= -x_c + y_c + z_c,\\
z_p &= x_c - y_c + z_c.
\end{aligned} \tag{8}$$

The primitive $R3c$ structure of α-$Li_4B_7O_{12}Cl$ contains two formula units per primitive cell or 48 atoms while the conventional cell contains eight formula units or 192 atoms. In order to assess how this computed structure compares with experiment, we show in Fig. 3 the x-ray pattern deduced from the optimized structure compared with the x-ray pattern constructed from the analysis of Jeitschko and coworkers [8] for measurements at a temperature of 298 K, analyzed in terms of the $F\bar{4}3c$ space group.

The optimized structure of α-$Li_4B_7O_{12}Cl$ is visualized in the primitive cell and conventional cell settings in Fig. 4,

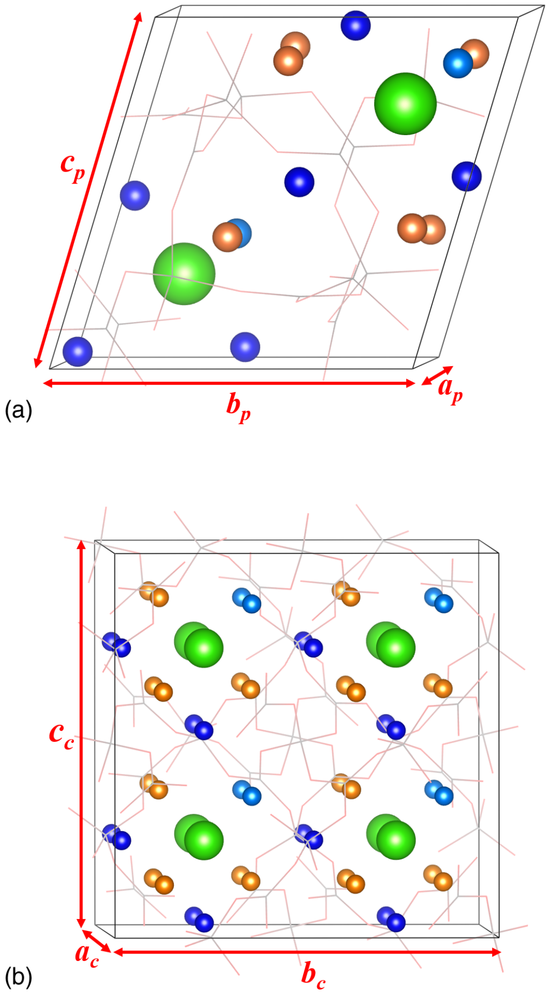

FIG. 4. Ball and stick diagram of $Li_4B_7O_{12}Cl$ in the (a) primitive and (b) conventional cell settings with the B-O framework represented by thin sticks and Cl indicated by green balls. The host Li ions with labels b and a are represented by dark blue and light blue balls, respectively. The unoccupied Li sites which serve as natural interstitials with Wyckoff label b are represented by brown balls.

TABLE I. Static lattice results in the conventional cell setting for $Li_4B_7O_{12}Cl$, comparing the fully optimized structure ("Full") with the optimized structure with cubic constraint ("Cubic") and various experimental results reported in Ref. [8]. The computed results also list ΔE (eV/FU), the estimate of the static lattice energy difference between the "Full" and "Cubic" optimizations.

	a_c (Å)	θ_c (deg)	ΔE (eV/FU)
Full	12.13	90.1	0.000
Cubic	12.14	90.0	0.002
Exp ($R3$)	12.141	90.083	
Exp ($F\bar{4}3c$ at 298 K)	12.141	90.0	
Exp ($F\bar{4}3c$ at 328 K)	12.161	90.0	
Exp ($F\bar{4}3c$ at 353 K)	12.167	90.0	

where the B-O framework is indicated with thin bonds so that the Li and Cl positions can be more easily visualized. In addition to the optimized Li ion sites indicated in this diagram, natural Li interstitial sites are also indicated, as explained in more detail below.

A summary of computed static lattice parameters of α-$Li_4B_7O_{12}Cl$ is given in Table I based on the conventional unit cell. In this case, we see that while the optimized structure of α-$Li_4B_7O_{12}Cl$ is definitely rhombohedral, the rhombohedral angle θ_c is very close to the ideal cubic angle of 90 deg. We can also optimize a constrained rhombohedral structure with $\theta_c = 90$ deg. The result, which is also listed in Table I, is very slightly higher energy than the unconstrained optimization [36].

In order to examine the structure of α-$Li_4B_7O_{12}Cl$ in more detail, we note that the face-centered rhombohedral structure $R3c$ and the face-centered cubic structure $F\bar{4}3c$ are very closely related in that the former is a subgroup of the latter. The Wyckoff labels and fractional coordinates of the primitive cells for these two space groups are detailed in Tables VI and VII in Appendix A. From the comparison of these tables, it is possible to map the cubic coordinates and Wyckoff labels of the $F\bar{4}3c$ structure to rhombohedral coordinates and Wyckoff labels of the $R3c$ structure as given in Table VIII (Appendix A). Most interestingly for this case, only the e label of the $F\bar{4}3c$ structure maps to both a and b labels of the $R3c$ structure while all of the other labels of the $F\bar{4}3c$ structure map exclusively to either the a or b labels of the $R3c$ structure.

The optimized structure of α-$Li_4B_7O_{12}Cl$ corresponds to Li sites analyzed in the $F\bar{4}3c$ structure with Wyckoff label e with the fractional occupancy of 25%, which in the $R3c$ structure corresponds to full occupancy of the Wyckoff site labeled a. This implies that the remaining six sites, corresponding the Wyckoff label b, should be available as natural vacancies in this structure. Representative fractional coordinates for the computed $R3c$ structure of $Li_4B_7O_{12}Cl$ are given in Table II together with the corresponding coordinates based on the $F\bar{4}3c$ analysis, using the primitive cell coordinates for both. We see significant agreement between the two structures. In addition to the occupied lattice sites, the analysis finds six natural interstitial Li sites which correspond to three quarters of the 8e sites in the $F\bar{4}3c$ setting which map to 6b sites in the $R3c$ setting. The typical method of identifying interstitial sites in a crystal is to carry out a systematic search of positions throughout the crystal for low-energy sites, which optimize the ideal structure with the addition of one Li ion and a uniform compensation charge. We performed this search for the α-$Li_4B_7O_{12}Cl$ structure and found the lowest energy interstitial sites to be quite close to the ideal 6b sites. In Table II, a representative ideal site is listed in the table and the computed interstitial is listed in the table note.

These static lattice optimization studies provide strong evidence that the ground-state structure of α-$Li_4B_7O_{12}Cl$ is face-centered $R3c$. The results also suggest that an idealized rhombohedral structure, optimized with the constraint that $\theta_p = 60$ deg and $\theta_c = 90$ deg, may be a good model for the β structure of the boracite. The notion that β-$Li_4B_7O_{12}Cl$ has the $R3c$ structure with $\theta_p = 60$ deg and $\theta_c = 90$ deg makes it identical with $F\bar{4}3c$ structure with special quarter occupancy of the Li(2) 8e sites suggested by Table VIII (see Appendix A). This would also be consistent with the notion that the higher temperature γ-$Li_4B_7O_{12}Cl$ phase has the

TABLE II. Representative primitive cell fractional coordinates for $Li_4B_7O_{12}Cl$, comparing the optimized $R3c$ structure (left) with the experimental analysis of single crystal data measured at 298 K based on the $F\bar{4}3c$ structure from Ref. [8].[a] Here "Label" refers to the primitive cell multiplicity and the Wyckoff label with "Occ." represents the corresponding number of occupied sites.

		$R3c$				$F\bar{4}3c$	
Atom	Label	Occ.	(x_p, y_p, z_p)	Atom	Label	Occ.	(x_p, y_p, z_p)
Li(1)	$6b$	6	(0.035, 0.036, 0.465)	Li(2)	$6c$	6	(0.000, 0.000, 0.500)
Li(2)	$2a$	2	(0.869, 0.869, 0.869)	Li(1)	$8e$	2	(0.871, 0.871, 0.871)
Li(i)[b]	$6b$	0	(0.869, 0.869, 0.393)				(0.871, 0.871, 0.388)
B(1)	$6b$	6	(0.251, 0.261, 0.753)	B(1)	$6d$	6	(0.250, 0.250, 0.750)
B(2)	$2a$	6	(0.602, 0.602, 0.603)	B(2)	$8e$	8	(0.600, 0.600, 0.600)
B(3)	$6b$	6	(0.109, 0.109, 0.698)				(0.100, 0.100, 0.699)
O(1)	$6b$	6	(0.438, 0.613, 0.757)	O(1)	$24h$	24	(0.439, 0.606, 0.757)
O(2)	$6b$	6	(0.447, 0.766, 0.197)				(0.439, 0.757, 0.198)
O(3)	$6b$	6	(0.187, 0.772, 0.615)				(0.198, 0.757, 0.606)
O(4)	$6b$	6	(0.712, 0.942, 0.106)				(0.698, 0.939, 0.106)
Cl	$2a$	2	(0.250, 0.250, 0.250)	Cl	$2b$	2	(0.250, 0.250, 0.250)

[a] Similar but not identical experimental results were reported in Ref. [17].

[b] Interstitial Li coordinate estimated as the coordinate $(x, x, -3x)$ as suggested from Table VII. Corresponding optimized Li interstial site was found to have coordinates (0.876, 0.880, 0.400).

$F\bar{4}3c$ structure with fractional occupancy on both the Li(1) $6c$ sites and the Li(2) $8e$ sites as established from the single-crystal analyses of Jeitschko and coworkers [8]. While this suggestion for the structure of the intermediate β phase seems reasonable from the group theory and geometric viewpoints, the actual intermediate structure may be more complicated. The suggestion by Jeitschko and coworkers [8] that the β structure has $P\bar{4}3n$ (no. 218) symmetry is, however, hard to imagine since this would require a transition between a face-centered rhombohedral lattice and a primitive cubic lattice as the crystal transforms from the α to β phase and a transition between a primitive cubic lattice and a face-centered cubic lattice as the crystal transforms from the β to γ phase.

B. $Li_5B_7O_{12.5}Cl$

There are several literature reports [6,16,17] focused on studying the effects of filling the natural interstitial sites in $Li_4B_7O_{12}Cl$ by forming solid solutions with Li_2O with the composition $Li_{4+x}B_7O_{12+x/2}Cl$ for $0 \leqslant x \leqslant 1$. The most concentrated material has the stoichiometry $Li_5B_7O_{12.5}Cl$, which was found to crystallize in the ordered face-centered cubic space group $F23$ (no. 196) [16] shown in Fig. 5. Interestingly, the space group $F23$ is a subgroup of the space group $F\bar{4}3c$ and the structures of $Li_5B_7O_{12.5}Cl$ and $Li_4B_7O_{12}Cl$ are closely related [37]. Table III shows the comparison of representative fractional coordinates of the two structures based on the experimental data of Refs. [8,16] in the conventional cell settings. The table shows quantitative agreement for the fully occupied B, O, and Cl sites of the two structures. Additionally, $Li_5B_7O_{12.5}Cl$ accommodates four extra O ions at $4a$ sites in the $F23$ structure. There is also good correspondence between the two structures in the positions of Li ions in $24g$ sites of the $F23$ structure and those in the higher symmetry $24c$ sites of the $F\bar{4}3c$ structure. The eight remaining Li ions in $Li_4B_7O_{12}Cl$ and the eight extra Li ions in $Li_5B_7O_{12.5}Cl$ are accommodated in $16e$ sites of the $F23$ structure which are closely related to half of the $32e$ sites of the $F\bar{4}3c$ structure. This leaves

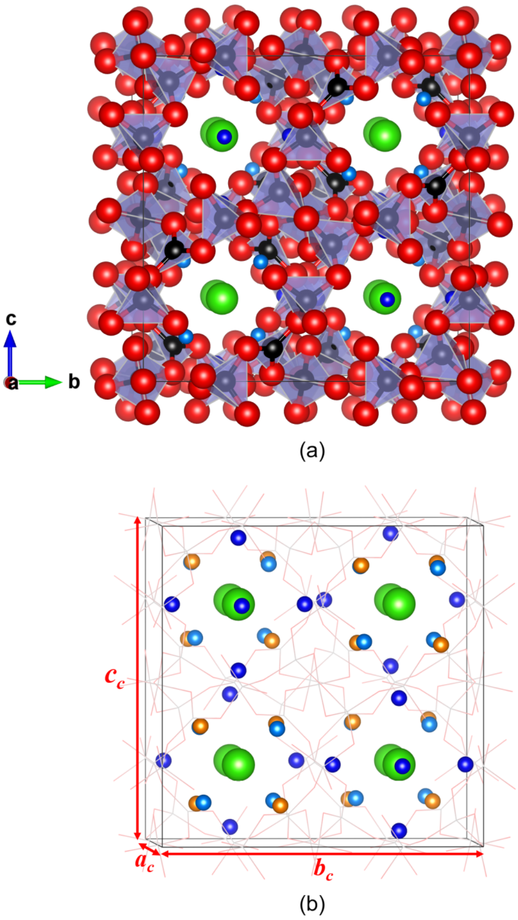

FIG. 5. (a) Ball and stick diagram of conventional cell of $Li_5B_7O_{12.5}Cl$ in the $F23$ structure. Ball colors of blue, black, red, and green indicate Li, B, O, and Cl ions, respectively. (b) Thin stick representation of B-O framework to fully display the positions of host Li sites (dark blue for $24g$ and light blue for $16e$) and the lowest energy interstitial Li sites (brown for $16e$).

TABLE III. Representative conventional cell fractional coordinates for the 204 ions of $\mathrm{Li_5B_7O_{12.5}Cl}$ in the $F23$ space group from the room-temperature experimental analysis of Ref. [16] compared with corresponding conventional cell fractional coordinates for the 192 ions of $\mathrm{Li_4B_7O_{12}Cl}$ in the space group $F\bar{4}3c$ structure from the experimental analysis of Ref. [8] (which are similar but not identical experimental results reported by Ref. [17]). Here "Label" refers to the conventional cell multiplicity and the Wyckoff label with "Occ." represents the corresponding number of occupied sites of the ideal structures at low temperature.

$\mathrm{Li_5B_7O_{12.5}Cl}$ ($F23$)				$\mathrm{Li_4B_7O_{12}Cl}$ ($F\bar{4}3c$)			
Atom	Label	Occ.	(x_c, y_c, z_c)	Atom	Label	Occ.	(x_c, y_c, z_c)
Li(1)	24g	24	(0.250, 0.250, 0.042)	Li(2)	24c	24	(0.250, 0.250, 0.000)
Li(2)	16e	16	(0.865, 0.865, 0.865)	Li(1)	32e	8	(0.871, 0.871, 0.871)
Li(i)[a]	16e	0	(0.365, 0.365, 0.365)				(0.371, 0.371, 0.371)
B(1)	24f	24	(0.000, 0.000, 0.252)	B(1)	24d	24	(0.000, 0.000, 0.250)
B(2)	16e	16	(0.081, 0.081, 0.081)	B(2)	32e	32	(0.100, 0.100, 0.100)
B(3)	16e	16	(0.601, 0.601, 0.601)				(0.600, 0.600, 0.600)
O(1)	48h	48	(0.020, 0.097, 0.181)	O(1)	96h	96	(0.023, 0.098, 0.182)
O(2)	48h	48	(0.023, 0.183, 0.599)				(0.023, 0.182, 0.598)
O(3)	4a	4	(0.000, 0.000, 0.000)				
Cl(1)	4c	4	(0.250, 0.250, 0.250)	Cl	8b	8	(0.250, 0.250, 0.250)
Cl(2)	4d	4	(0.750, 0.750, 0.750)				(0.750, 0.750, 0.750)

[a] Coordinates deduced from corresponding $F\bar{4}3c$ symmetry.

16 natural Li ion vacancies at shifted 16e sites in the $F23$ structure which are related to 24 natural interstitial sites of the $F\bar{4}3c$ structure associated with the 1/4th occupied 32e sites in $\mathrm{Li_4B_7O_{12}Cl}$.

The computational results for the lattice constant and fractional coordinates of the optimized structure of $\mathrm{Li_5B_7O_{12.5}Cl}$ are listed in Table IV. The computed fractional coordinates of the occupied sites agree within ±0.002 the results of Ref. [16] listed in Table III. In addition to the optimized occupied sites, the optimized coordinate of the lowest energy interstitial Li site is also given.

TABLE IV. The optimized structure of $\mathrm{Li_5B_7O_{12.5}Cl}$ in the face centered cubic space group $F23$ with lattice constant $a_c = 12.106$ Å is compared with the room temperature experimental analysis of Ref. [16] with lattice constant $a_c = 12.136$ Å. In this table, for each distinct **Atom**, **Label** refers to the conventional cell multiplicity and the Wyckoff label with **Occ.** representing the corresponding number of occupied sites of the ideal structures at low temperature with the computed representative fractional coordinates (x_c, y_c, z_c). The computed fractional coordinates can be compared with the corresponding experimental conventional cell fractional coordinates listed in Table III.

Atom	Label	Occ.	(x_c, y_c, z_c)
Li(1)	24g	24	(0.250, 0.250, 0.043)
Li(2)	16e	16	(0.865, 0.865, 0.865)
Li(i)[a]	16e	0	(0.374, 0.374, 0.374)
B(1)	24f	24	(0.000, 0.000, 0.251)
B(2)	16e	16	(0.081, 0.081, 0.081)
B(3)	16e	16	(0.601, 0.601, 0.601)
O(1)	48h	48	(0.018, 0.098, 0.180)
O(2)	48h	48	(0.022, 0.183, 0.600)
O(3)	4a	4	(0.000, 0.000, 0.000)
Cl(1)	4c	4	(0.250, 0.250, 0.250)
Cl(2)	4c	4	(0.750, 0.750, 0.750)

[a] Determined by optimizing system with extra Li ion.

As seen from the ball and stick drawing of eight formula units of the conventional cell illustrated in Fig. 5(a), the rigid three-dimensional B-O framework made up of interconnected $\mathrm{BO_3}$ triangles and $\mathrm{BO_4}$ tetrahedra is similar to that of other boracites. Notably, $\mathrm{Li_5B_7O_{12.5}Cl}$ contains extra O ions of O(3) type fully occupying 4a sites at (0.000, 0.000, 0.000), while the corresponding position is empty in cubic $F\bar{4}3c$ models of $\mathrm{Li_4B_7O_{12}Cl}$. Figure 5(b) highlights the arrangement of Li ions, including two distinct hosts and the lowest energy metastable interstitial sites as indicated by two shades of blue and brown balls, respectively. Within the conventional cell, the computed interstitial sites have Wyckoff labels 16e and are located at fractional positions equivalent to (0.374, 0.374, 0.374).

In addition to these differences in the O ion positions, the ordering of Li ions is also responsible for the change in symmetry from $R3c$ structure of $\mathrm{Li_4B_7O_{12}Cl}$ to $F23$ structure of $\mathrm{Li_5B_7O_{12.5}Cl}$. On the other hand, it is interesting to analyze the correlations between the Li ions in these two materials. Specifically, the Li sites with Wyckoff labels 24g in the cubic $\mathrm{Li_5B_7O_{12.5}Cl}$ have a one-to-one correspondence with those at 4 × 6b sites in the conventional cell of rhombohedral $\mathrm{Li_4B_7O_{12}Cl}$. The case of the e type sites is less immediately apparent. It is found that the 16e type host sites of $\mathrm{Li_5B_7O_{12.5}Cl}$ together with its lowest energy metastable interstitial sites can map to eight host and 24 vacant sites in the rhombohedral $\mathrm{Li_4B_7O_{12}Cl}$.

IV. LATTICE VIBRATIONS

The calculation of vibrational properties follows the methods discussed in detail in a previous study [39]. The phonon dispersion relations of $\mathrm{Li_4B_7O_{12}Cl}$ and $\mathrm{Li_5B_7O_{12.5}Cl}$, both calculated in the primitive cell setting, together with the corresponding projected atomic density of states are shown in

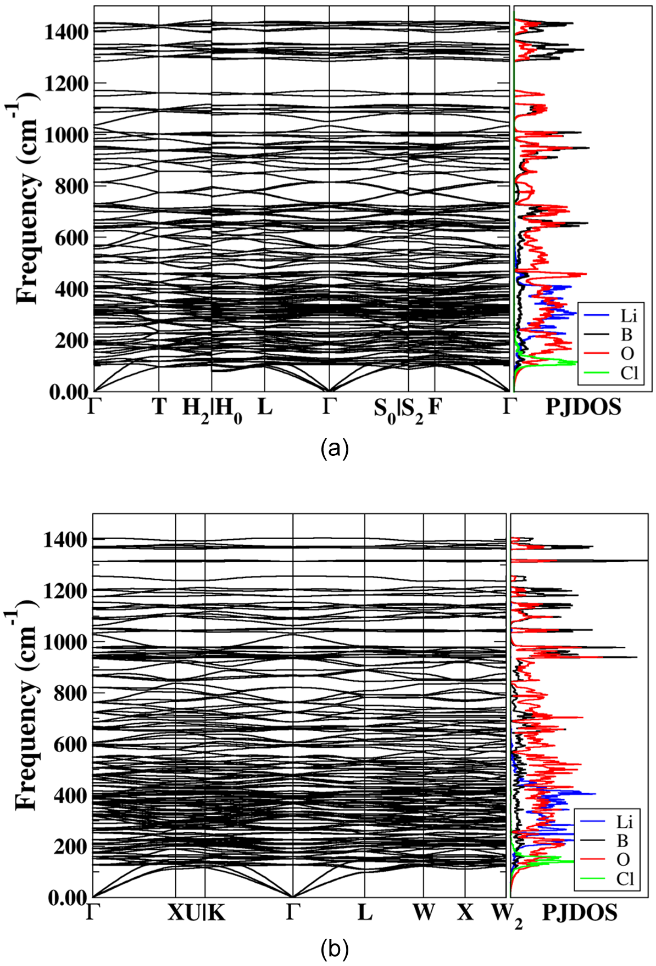

(a)

(b)

FIG. 6. Calculated phonon spectrum along high-symmetric crystallographic directions and their corresponding projected densities of states for each atom type (PJDOS) for (a) $Li_4B_7O_{12}Cl$ and (b) $Li_5B_7O_{12.5}Cl$. The range of the PJDOS plots was fixed at the maximum PJDOS value for $Li_5B_7O_{12.5}Cl$. The high-symmetry **q** lines were selected according to the recommendation from Ref. [38] for each particular space group. For the $R3c$ structure of panel (a), the labels refer to the equivalent hexagonal structure, while for the $F23$ structure of panel (b), the labels refer to the standard face-centered cubic structure.

Fig. 6, suggesting very similar profiles for the two crystals. For $Li_4B_7O_{12}Cl$, which has 48 atoms per primitive cell, the total number of lattice vibrational modes is 144. The highest frequency is computed to be 1435 cm^{-1}. With the atomic motion assigned to symmetry under the $C_{3v}(3m)$ point group, the zone center acoustic and optic normal modes break into the following irreducible components [1]:

$$\Gamma^{R3c}_{\text{acoustic}} = \mathrm{A}_1 + \mathrm{E},$$
$$\Gamma^{R3c}_{\text{optic}} = 23\mathrm{A}_1 + 24\mathrm{A}_2 + 47\mathrm{E}. \qquad (9)$$

Here the A modes are due to a nondegenerate vibration with the subscripts 1 and 2 indicating symmetric and antisymmetric with respect to the principal rotation axis, respectively; E denotes the doubly degenerate modes. Further group theoretical analysis finds that among the three types of optical modes, the 23 A_1 and 47 E optical modes simultaneously belong to infrared active and Raman active modes as well. The situation suggests that, without considering the three silent acoustic modes, a vibration associated with the A_1 or E type mode leads to change in both dipole moment and polarizability, while the 24 remaining A_2 modes are normal optical modes with no particular attribution.

For $Li_5B_7O_{12.5}Cl$, which has 51 atoms per primitive cell, the total number of phonon modes is 153 with the highest frequency computed to be 1404 cm^{-1}. Due to relatively higher symmetry, the dispersion curves of $Li_5B_7O_{12.5}Cl$ in the $F23$ structure display more degeneracy. Depending on symmetries originating from point group $T(23)$, the zero center phonon modes decompose into irreducible representations [1] as follows:

$$\Gamma^{F23}_{\text{acoustic}} = \mathrm{T},$$
$$\Gamma^{F23}_{\text{optic}} = 11\,\mathrm{A} + 11^1\mathrm{E} + 11^2\mathrm{E} + 39\,\mathrm{T}. \qquad (10)$$

Here the notation T represents the triply degenerate modes in a three-dimensional crystal system. Further symmetry analysis finds the Raman active modes $\Gamma_{\text{Raman}} \equiv \Gamma_{\text{optic}}$ in Eq. (10), whereas the infrared active modes only include the T type modes.

In both materials, there are no imaginary phonon modes exhibited, indicating that each crystal structure is dynamically stable. Whereas the primary involvement of Li motion occurs in the lower frequency modes in the range of 0–600 cm^{-1}, the higher frequency modes are predominately attributed to motions of the B and O ions. In particular, the B(1) type ions located in the center of the planar B-O triangles are found to have relatively larger vibrational amplitudes in the top branches with mode indices 129–144 and frequencies ranging from 1285 to 1434 cm^{-1}. It is also interesting to note that the vibration modes involving appreciable Cl ion motion have an even lower of frequency less than 240 cm^{-1}, which is perhaps not surprising because of the "immobility" of the massive Cl ions and weak bonding strength of Cl with other ions. The vibrational modes were also analyzed for the constrained rhombohedral lattice with $\theta_p = 60$ deg (corresponding to the one labeled "Cubic" in Table I), finding indistinguishable phonon dispersion curves from those of the fully optimized rhombohedral structure shown in Fig. 6(a).

Having established that both $Li_4B_7O_{12}Cl$ and $Li_5B_7O_{12.5}Cl$ are dynamically stable in their ground-state structures, it is possible to study their stability more quantitatively by estimating their Helmholz free energies. For well-ordered and electronically insulating crystalline material, it is reasonable to approximate the Helmholtz free energy as a function of temperature T to be

$$F(T) = U_{\text{SL}} + F_{\text{vib}}(T). \qquad (11)$$

Here U_{SL} represents the temperature-independent static lattice energy which is well approximated by the total energy of the DFT calculation of the optimized structure. The phonon free energy $F_{\text{vib}}(T)$ is obtained by integrating the phonon density of states over the whole frequency range, which is essential to quantify the contributions of the lattice vibrations as described (for example) in Eqs. (1)–(4) of Ref. [40]. This can be done for $Li_4B_7O_{12}Cl$ and $Li_5B_7O_{12.5}Cl$ from the phonon results illustrated in Fig. 6.

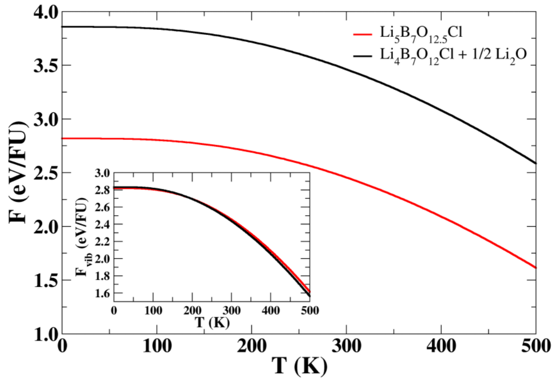

FIG. 7. Plot of Helmholtz free energy and the vibrational free energy (inset) for the left- and right-hand side components of Eq. (12).

For example, consider the following transformation:

$$\mathrm{Li_5B_7O_{12.5}Cl \rightarrow Li_4B_7O_{12}Cl + 1/2\,Li_2O.} \qquad (12)$$

We can compare the Helmholtz free energies of both sides of Eq. (12). In addition to contributions from $Li_4B_7O_{12}Cl$ and $Li_5B_7O_{12.5}Cl$, the static lattice energy and phonon spectrum of Li_2O in its antiflorite structure [41] was also calculated. The results are shown in Fig. 7, suggesting that $Li_5B_7O_{12.5}Cl$ is more stable than separate crystals of $Li_4B_7O_{12}Cl$ and Li_2O throughout the temperature range considered. However, in the absence of excess Li_2O, lithium boracite $Li_4B_7O_{12}Cl$ is expected to be stable. Additionally, the embedded plot of $F_{\mathrm{vib}}(T)$ in Fig. 7 shows that the vibrational energy difference between the two sides of Eq. (12) is trivial across the explored temperature range. For this system, the Helmholtz free energy difference is dominated almost exclusively by the static lattice energy part. For example, at 300 K, the vibrational energy difference is $F_{\mathrm{vib}}(\mathrm{Li_4B_7O_{12}Cl}) + 1/2F_{\mathrm{vib}}(\mathrm{Li_2O}) - F_{\mathrm{vib}}(\mathrm{Li_5B_7O_{12.5}Cl}) =$ 0.02 eV/FU, while the corresponding static lattice energy difference is 1.0 eV/FU.

V. STABILITY ANALYSIS

The phase stability of the crystal structures of $Li_4B_7O_{12}Cl$ and $Li_5B_7O_{12.5}Cl$ was also evaluated using the convex hull approach [42], which is based on the idea that the phase stability of a crystal structure can be determined from the energy of its components. Within this framework, the stability of a compound requires it to be on a convex hull construction composed of a set of tie lines that connect all the related lowest energy phases [43]. Also, a compound lying on the convex hull suggests that it has lower energy than the stoichiometric linear combinations of other phases in the system with the same composition.

In the present study, it is convenient to construct the convex hull analysis using the building blocks of Li_2O, B_2O_3, and LiCl which span the composition space of $Li_4B_7O_{12}Cl$, $Li_5B_7O_{12.5}Cl$, and many of their possible decomposition products. For this analysis, we focus on the DFT static ground-state energies. With the effort of computing phonon properties, it is possible to perform a more advanced stability analysis at given temperatures. However, it is evident from Fig. 7 that the pure phonon energy is less likely to change the qualitative picture of the stability properties of the materials. Therefore, the finite-temperature vibrational effects were not taken into account in this analysis. Accordingly for each material, we calculate the energy difference

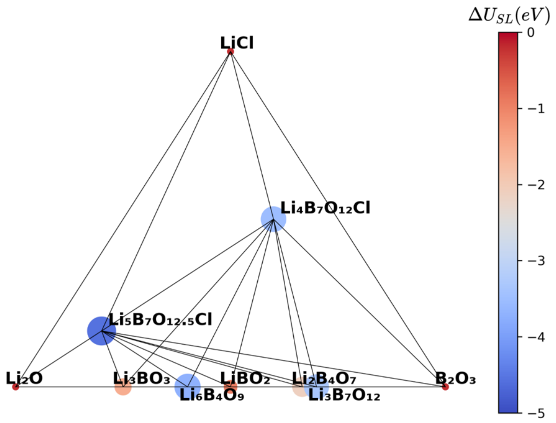

FIG. 8. Convex hull of the Li_2O-B_2O_3-LiCl system with filled colored circles indicating values of the energy differences ΔU_{SL} as defined in Eq. (13) for each of the stable phases. The color bar indicates the values of ΔU_{SL} in units of eV/formula unit. Additionally, the circle radii are drawn in proportion to the magnitudes of $|\Delta U_{\mathrm{SL}}|$.

$$\Delta U_{\mathrm{SL}} = U_{\mathrm{SL}} - \sum_{i=1}^{3} x_i U_{\mathrm{SL}}^{i}, \qquad (13)$$

where U_{SL} is the total static energy per formula unit of a specific compound, and U_{SL}^{i} is the total static energy per formula unit of the reference compounds with indices $i = \mathrm{Li_2O}$, B_2O_3, and LiCl. The compositional parameters x_i are chosen such that the specific compound and the sum of the reference compounds have the same atomic composition.

Results for the convex hull diagram based on the ternary Li_2O-B_2O_3-LiCl composition space is presented in Fig. 8. The energy difference of each stable phase was calculated according to Eq. (13) and is represented by a node on the diagram. For each node, its color and size represents the value and magnitude, respectively, of ΔU_{SL}. The computed values of ΔU_{SL} are enumerated in Table IX in Appendix B. Although the results show that $Li_5B_7O_{12.5}Cl$ is relatively more stable than $Li_4B_7O_{12}Cl$ in terms of decomposing into the three reference compounds Li_2O, B_2O_3, and LiCl, $Li_4B_7O_{12}Cl$ is unlikely to react without excess Li_2O. In other words, by controlling the weight fraction of precursor constituents, the results are consistent with the experimental findings that it is possible to synthesize crystals of $Li_4B_7O_{12}Cl$.

VI. MECHANISMS FOR LI ION MIGRATION

In Sec. III, we established that the structures of both $Li_4B_7O_{12}Cl$ and $Li_5B_7O_{12.5}Cl$ have a significant number of natural interstitial sites available to Li ions. Within the conventional cell setting, for $Li_4B_7O_{12}Cl$ with 192 ions, there are 24 of these natural interstitial sites. Correspondingly for $Li_5B_7O_{12.5}Cl$ with 204 ions, there are 16 of these natural

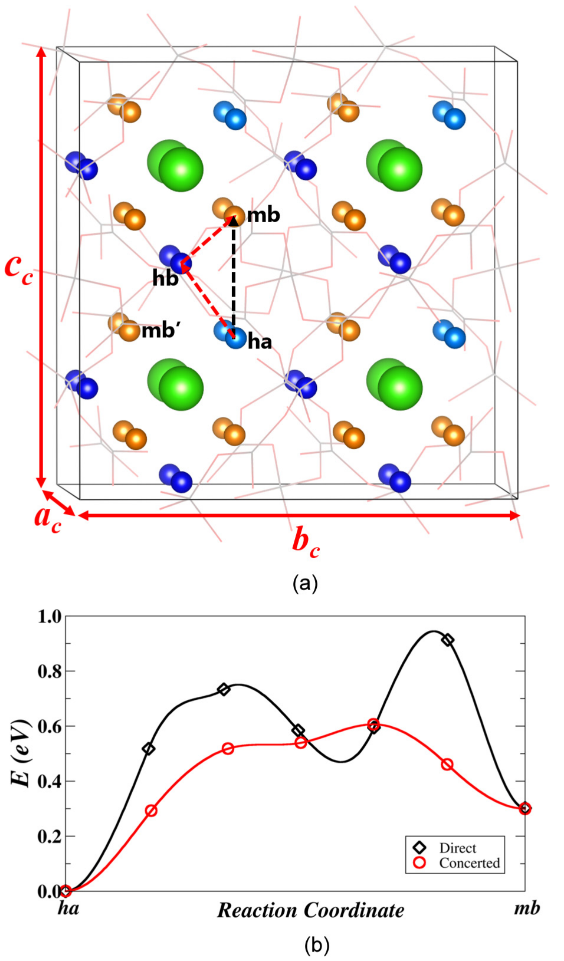

FIG. 9. (a) Ball and stick diagram of Li ion sites of $Li_4B_7O_{12}Cl$ with the migration path indicated with arrows and by labels (*ha*, host *a* site; *hb*, host *b* site; *mb* and *mb*′, metastable *b* sites). (b) NEB energy path diagram for the direct (black) and concerted (red) Li ion migration processes.

interstitial sites. Using both the nudged elastic band (NEB) approach [44–46] and molecular dynamics simulations, we can examine how these may or may not participate in Li ion diffusion.

A. The nudged elastic band simulations

Using the NEB method, we estimated the migration energies E_m of Li ion diffusion for several most likely paths in $Li_4B_7O_{12}Cl$ and $Li_5B_7O_{12.5}Cl$.

1. $Li_4B_7O_{12}Cl$

For the case of $Li_4B_7O_{12}Cl$, it is reasonable to speculate that the metastable *b* type site (based on the $R3c$ space group) may play an essential role in the course of Li ion transport as they are native interstitials in the simulation cell. Here host *a* type and metastable *b* type sites are all derived from the *e* type sites of the $F\bar{4}3c$ structure. All calculations were carried out using the 192 ion conventional cell of the $R3c$ structure as visualized in Fig. 9. Figure 9(a) shows sites considered in this analysis, involving a natural interstitial at a metastable *b* site (labeled *mb*) and nearest neighbor host Li sites host *a* (labeled *ha*) and host *b* (labeled *hb*). Using the structural optimization algorithms in the QUANTUM ESPRESSO software we find that the direct migration of *hb* → *mb* is not stable, while the migration of *ha* → *mb* is metastable with an energy gain of 0.30 eV. Furthermore, we found that the host *b* type sites (*hb*) are the most stable positions for accommodating Li ions. Once such a site is vacant, the Li ion at adjacent host *a* site (*ha*) or metastable *b* site (*mb*) will immediately hop into this available position.

From these results, there are two possible migration paths. One possibility, called the "direct" hop, is the process *ha* → *mb*. Another possibility, called the "concerted" hop involves the same final configuration but involves a concerted motion of *hb* → *mb* simultaneously with the motion of *ha* → *hb*. These two paths were analyzed using the NEB method with the corresponding migration energy diagrams shown in Fig. 9(b).

By comparison, the concerted hop has migration energy E_m of 0.61 eV, lower by about 0.33 eV than the direct hop. Interestingly, the direct migration is found to be accompanied by a local minimum located near the third NEB image of the energy diagram. Further inspection revealed that, instead of hopping in the direction toward the *mb* site, the active Li ion originating from site *ha* appears to be attracted by the host site *hb* and attempts to occupy this low-energy position by kicking the currently resting Li ion out to a metastable site labeled with *mb*′ in the diagram, causing the special intermediate configuration with locally minimal energy. Because of the NEB algorithm in which the final state is well-defined, the intermediate configuration involving the *mb*′ site is not realized in the direct hop simulation; the Li ion now at *hb* continues to move to site *mb* and the one at *mb*′ also returns back to site *hb*. While for the concerted migration, the process consists of two simultaneous hopping events consisting of *hb* → *mb* and *ha* → *hb* as described before. We find that, within the NEB algorithm, the first hop progresses much faster than the second one. In other words, when the Li ion originating in the *hb* site jumps into the target position *mb*, the other host Li ion has just left its original position of site *ha*.

As discussed above, even in the direct Li ion migration between *ha* and *mb*, the participation of the third type site *hb* was observed. What the direct and the concerted migrations have in common is that the motions of the Li ions at the *a* type host sites *ha* will instantly affect the states of the Li ions at *hb* type sites, as they will be promptly stimulated to hop into an available metastable site in the vicinity. It is, therefore, reasonable to speculate that the concerted migration involving two distinct host sites and a metastable site dominates the Li ion transport in $Li_4B_7O_{12}Cl$.

2. $Li_5B_7O_{12.5}Cl$

For the case of $Li_5B_7O_{12.5}Cl$, the smallest distance between natural interstitial sites is greater than 4.30 Å, so the Li ion migration involving these sites is less likely. Consequently, it is speculated that a vacancy process may play a dominant role in Li ion transport. Each vacancy defect configuration is modeled by directly removing a Li ion from the host site while

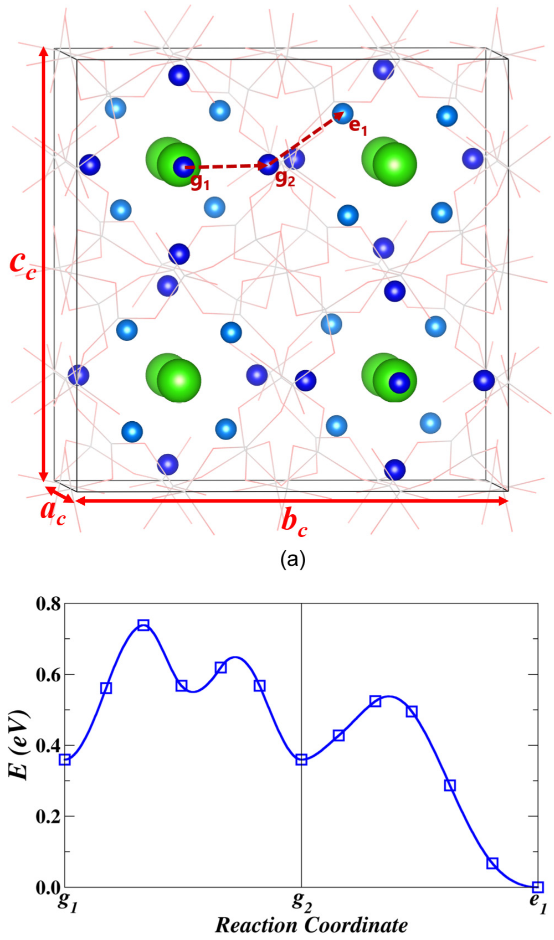

(a)

(b)

FIG. 10. (a) Ball and stick diagram of $Li_5B_7O_{12.5}Cl$ with the Li ions migration pathway indicated by labels and arrows. (b) NEB energy path diagram for this vacancy mechanism.

adding a compensating uniform charge of the opposite sign to the system.

It is found that the most efficient Li ion conduction path within the supercell consists of the relatively short hops between neighboring g type sites with a distance of 3.54 Å and those between adjacent g and e type sites [47] at a distance of 2.92 Å apart. One example of the smallest path unit is indicated by the labels on these three Li sites in Fig. 10(a). Multiple energetically equivalent paths with such patterns expand in all directions, connecting to form continuous paths throughout the crystal.

Figure 10(b) shows the corresponding NEB energy diagram with the zero of the energy was taken as the energy of the Li ion vacancy at a site of e type. It shows the vacancies g_1 and g_2 of the same g type have vacancy defect energy higher by about 0.36 eV than the e type vacancy. The overall migration energy E_m is determined by the maximum energy difference along the path which is $E_m = 0.75$ eV. Taking into account the contribution of the defect formation energy needed to produce a mobile Li ion, the activation energy E_a for Li ion conductivity is estimated to be 1.06 eV according to the relation $E_a = E_m + \frac{1}{2}E_f$. The high activation energy indicates that $Li_5B_7O_{12.5}Cl$ is expected to have poor Li ion conductivity.

B. Molecular dynamics simulation

The statistical behavior of Li ion diffusion in $Li_4B_7O_{12}Cl$ and $Li_5B_7O_{12.5}Cl$ was investigated using *ab initio* molecular dynamics (MD) simulation, which allows for directly simulating the dynamical diffusion of Li ions in real time. These simulations are likely to reveal more details of the ionic transport mechanisms. The simulations were carried out for a microcanonical NVE ensemble with a time integration step of $\Delta t = 2.4$ fs for conventional unit cells of $Li_4B_7O_{12}Cl$ (containing 192 ions in the $R3c$ structure) and $Li_5B_7O_{12.5}Cl$ (containing 204 ions in the $F23$ structure). For both materials, the simulations were carried out using the optimized static lattice lattice parameters, not taking into account the temperature-dependent lattice expansion or phase transformations. This approximation is weakly justified by the argument that larger errors in molecular dynamics simulations are likely to occur from other algorithmic approximations such as the initial randomized velocity distribution. The simulation temperature, as measured from the time averaged ion kinetic energy, was controlled by scaling the initial randomized ion velocities. Typically, starting from the ideal ground-state geometry and setting the initial effective temperature to twice the target value, for each simulation the average temperature was found to be within 40 K of the target temperature and the root mean squared temperature fluctuation was found to be roughly 50 K.

Figure 11 illustrates the examples of the migration patterns of Li ions during MD simulations in each material. For the case $Li_4B_7O_{12}Cl$, it is not surprising to note that the *mb* type native vacant sites, represented by brown balls in Fig. 11(a), are frequently visited by the mobile Li ions in the course of diffusion. Careful examination of this visualization from different viewpoints finds that there is no direct hopping between the host *ha* and *mb* type sites. Instead, the most efficient pathway for conducting Li ions is composed of path segments between sites *hb* → *mb* and *ha* → *hb*. For the $Li_5B_7O_{12.5}Cl$ case, as displayed in Fig. 11(b), the fully presented Li ion positions of MD simulations are somewhat similar to those of $Li_4B_7O_{12}Cl$ as the ionic conduction mainly occurs in the hollow cavity formed by robust B-O units. Unlike in the nearly continuous diffusion pathway observed in the $Li_4B_7O_{12}Cl$ cell, we can see clearly that the Li ions exhibit comparatively low mobility, with most of them being trapped near their initial host sites. Besides, it seems that the interstitial defect sites, indicated by brown balls in the diagram, are not evolved in the Li ion diffusion process visualized in this simulation. Only a few Li ion hops take place between the neighboring host sites of g and e type which have a relatively shallow migration barrier energy as computed in the NEB analysis. However, those hopping events are localized and unable to achieve long-range conduction of Li ions. Generally, the MD simulation results on $Li_4B_7O_{12}Cl$ and $Li_5B_7O_{12.5}Cl$ are compatible with the NEB analysis in Sec. VI A.

To better analyze the molecular dynamics simulations, it is convenient to define a time-dependent site occupancy

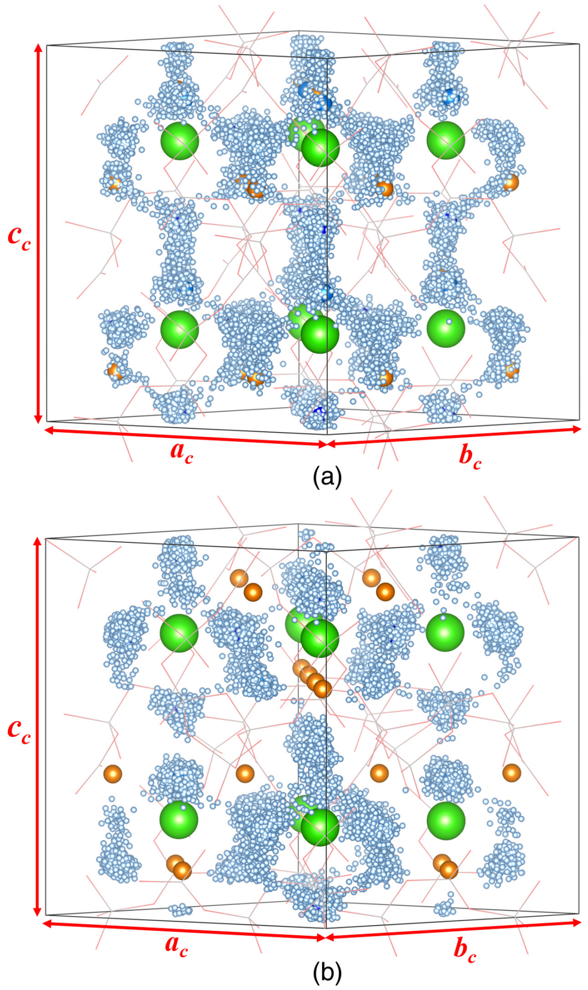

FIG. 11. Diagrams of MD simulations over $t = 50$ ps at intervals of $50\Delta t = 0.12$ ps for (a) $Li_4B_7O_{12}Cl$ at $\langle T \rangle = 1162$ K and (b) $Li_5B_7O_{12.5}Cl$ at $\langle T \rangle = 1171$ K. The little blue balls indicate the time-dependent positions of Li ions. The atomic positions of the initial configurations and natural vacancies are also shown, using the same color conventions as in Figs. 4(b) and 5(b), respectively.

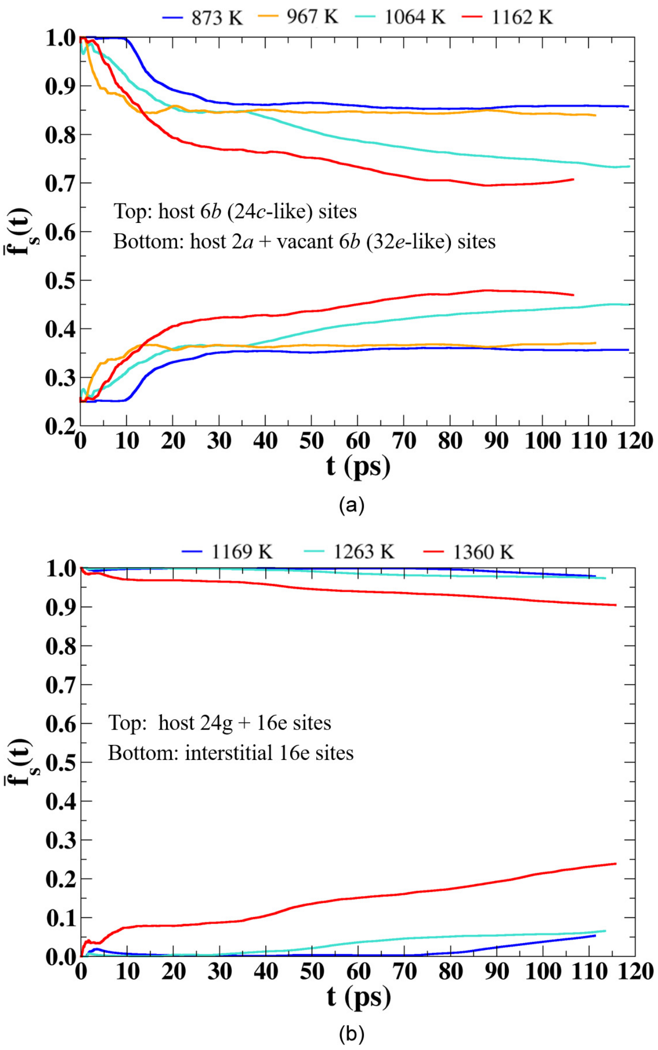

FIG. 12. Plots of $\bar{f}_s(t)$ as defined in Eq. (15) for (a) $Li_4B_7O_{12}Cl$ and (b) $Li_5B_7O_{12.5}Cl$. The subscript s of $f_s(t)$ denotes the reference site type as described in the text of each figure, using the Wyckoff labels of the $R3c$ and $F23$ structures as appropriate. The average temperature of each plot is listed in the legend.

factor $f_s(t)$

$$f_s(\mathrm{t}) = \frac{1}{N_s^{Li}} \sum_{i=1}^{N^{\mathrm{Li}}} n_s^i(t),\ i = 1, 2, \ldots, N^{\mathrm{Li}} \text{ and}$$

$$\sum_s N_s^{\mathrm{Li}} = N^{\mathrm{Li}}, \tag{14}$$

where N^{Li} is the total number of Li ions in the simulation cell and s denotes the reference site type: host a, b, and metastable b for $Li_4B_7O_{12}Cl$, and host g, e, and metastable e for $Li_5B_7O_{12.5}Cl$. N_s^{Li} indicates the multiplicity number of site s based on the conventional lattice. (Note that the conventional unit cell of the $R3c$ structure has four times as many ions as the primitive cell discussed in Sec. III A). At each time step t, the label of a Li ion is determined by the closest reference site relative to this ion's instantaneous position. The counter $n_s^i(t) = 1$ if the ith Li ion has the shortest distance with the reference site s; otherwise, $n_s^i(t) = 0$. Accordingly, $f_s(\mathrm{t})$ measures the occupation probability of s type site at t.

It is found that the curve of $f_s(\mathrm{t})$ is very noisy; as computed from the MD trajectories, the Li ion labels change rapidly. More conveniently, we can define a time-averaged site occupancy factor by integrating the instantaneous site occupancy over a time duration t

$$\bar{f}_s(\mathrm{t}) = \frac{1}{t} \int_0^t f_s(t')dt'. \tag{15}$$

Figure 12(a) shows the plot of $\bar{f}_s(\mathrm{t})$ for distinct sites of $Li_4B_7O_{12}Cl$ in the rhombohedral structure, comparing results at various temperatures ranging from 900 to 1200 K. Note that $t = 0$ corresponds to the ground-state configuration in which the $4 \times 6b$ sites of the $R3c$ structure, mapped from the $24c$ type sites of the ideal $F\bar{4}3c$ model, are fully occupied, whereas the occupancy of the remaining Li sites, mapped from the $32e$ type of the cubic cell, is 25%. As time progresses, $\bar{f}_s$ varies and tends to an asymptotic value at long times. It is also evident that the fractional occupancy of host $24c$ like sites decreases, and that of the $32e$ like sites increases at higher temperatures. In other words, at low temperatures the Li ions have a preference to reside in the most energetically favorable positions of $6b$ type. This phenomenon is consistent with what the experiment observed upon heating from the room-temperature α phase to the high-temperature phases. Since for this particular material, the MD temperatures are necessary to be high enough to overcome the migration barrier and therefore to achieve conduction of Li ions, the simulated value of site occupancy factor for the experimentally reported phase transition temperatures 310 K for α to β, and 348 K for β to γ are unattainable. Although the exact functional relationship between the temperature and the site fractional occupancy is unknown and undefined, the calculated $\bar{f}_s(t)$ curves appear to be qualitatively consistent with temperature-dependent x-ray analysis reported in Ref. [8].

For the case of $Li_5B_7O_{12.5}Cl$ with the calculated $\bar{f}_s(t)$ displayed in Fig. 12(b), we find that the role of the interstitial defects is nontrivial only at simulation temperature above 1300 K. Generally, most hop events occur between the host sites via vacancy diffusion process. While optimizing the electrolyte properties of $Li_5B_7O_{12.5}Cl$ is beyond the scope of the present work, it is proposed that, in view of the NEB analysis in Sec. VI A, the possible way to enhance the ionic conductivity of $Li_5B_7O_{12.5}Cl$ is by introducing vacancy defects in the lattice.

The ionic conductivity σ, a measure of the ability of a material to conduct ions, is related to the temperature dependent ionic diffusion coefficient $D(T)$ according to the Nernst-Einstein relationship

$$\sigma(T) = \rho q^2 \frac{D(T)}{k_B T}. \tag{16}$$

Here we assume that only Li ions having charge q contribute to the conductivity, ρ represents the average number density of mobile Li ions in the simulation cell, and k_B denotes the Boltzmann constant. Typically, the product $T\sigma$ follows an Arrhenius temperature of the form

$$T\sigma(T) = K e^{-E_a^{\mathrm{MD}}/k_B T}, \tag{17}$$

where K is a temperature-independent constant and E_a^{MD} the activation energy for Li ion conductivity. In practice, it is difficult to calculate the ionic diffusion coefficient from a molecular dynamics simulation, and it is approximated by computing the tracer diffusion coefficient, scaled by the Haven ratio H_r [48] according to

$$D(T) = D_{tr}(T)/H_r. \tag{18}$$

The tracer diffusion coefficient $D_{tr}(T)$ is calculated directly from the molecular dynamics trajectories in terms of the mean squared displacement as described, for example, in Eqs. (10) and (11) of Ref. [49]. In this work, all results are obtained by assuming $H_r = 1$. In order to check the mobility of ions other than Li, we calculated $D_{tr}(T)$ for the borate framework and Cl ions finding them to have negligible value even at high temperature. This result provides justification for focusing on the Li ion contributions alone. It also means that the borate and Cl ions provide a rather rigid framework in contrast to other electrolyte systems where rotations of complex anions play an important role in conduction mechanisms [50]. Results for the calculated conductivities are given in Fig. 13 and Table V, where they are compared with experimental results from the literature.

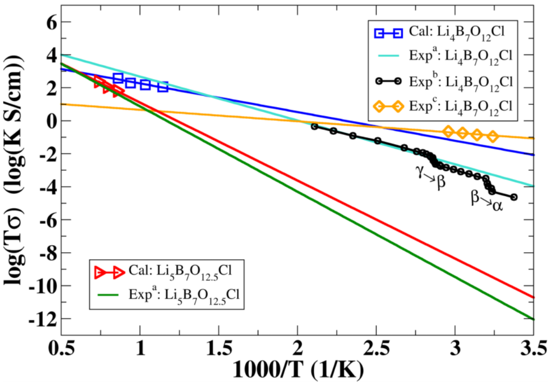

FIG. 13. Plots of simulated ionic conductivities of $Li_4B_7O_{12}Cl$ and $Li_5B_7O_{12.5}Cl$, together with the available experimental values obtained by digitizing the published graphs from Refs. [6] (a), [8] (b), and [12] (c). All straight lines represent least squares fits of the $\log(T\sigma)$ vs $1000/T$ data.

For the $Li_5B_7O_{12.5}Cl$ material, the calculated results on the perfect crystal are not far off from the experimental measurements on polycrystalline samples [6]. However, the higher activation barrier and the extremely low ionic conductivity at room temperature indicate that this material is an extremely poor ionic conductor. By contrast, both experiment and simulations find $Li_4B_7O_{12}Cl$ to be a viable ionic conductor. Interestingly the experimental results show considerable variability even among the few results presented here. The two early measurements [6,8] represented in turquoise and black in Fig. 13 are similar to each other, although more details are presented in the measurements of Ref. [8] including the phase transitions between two high-temperature cubic phases, and a low-temperature rhombohedral phase. The recent measurements of Ref. [12] represented in orange in Fig. 13 find room-temperature conductivity values two orders of magnitude higher than that of the earlier work, perhaps because of greater sample purity. The simulation results represented by blue points and straight line are in the approximate range of the diverse experimental values.

TABLE V. Comparison of activation energies (E_a^{MD}) and ionic conductivities (σ) at $T = 300$ K determined from fitting Arrhenius form to molecular dynamics simulations and to literature results.

Materials	Analysis	E_a^{MD} (eV)	σ(300 K) (S/cm)
$Li_4B_7O_{12}Cl$	Cal[a]	0.3	1×10^{-4}
	Exp[b]	0.1	4×10^{-4}
	Exp[c]	0.5	1×10^{-6}
$Li_5B_7O_{12.5}Cl$	Cal[a]	0.9	4×10^{-13}
	Exp[c]	1.0	2×10^{-14}

[a] This work.
[b] Ref. [12] (labeled "c" in Fig. 13).
[c] Ref. [6] (labeled "a" in Fig. 13).

TABLE VI. Wyckoff labels with multiplicity "Mul." and their fractional coordinates (x, y, z) for group $R3c$ (no. 161) in its primitive cell setting. In this case, (x, y, z) refers to the primitive lattice coordinates (x_p, y_p, z_p).

Mul.	**Label**	**Fractional coordinates**
6	b	(x, y, z) (z, x, y) (y, z, x) $\left(z + \frac{1}{2}, y + \frac{1}{2}, x + \frac{1}{2}\right)$ $\left(y + \frac{1}{2}, x + \frac{1}{2}, z + \frac{1}{2}\right)$ $\left(x + \frac{1}{2}, z + \frac{1}{2}, y + \frac{1}{2}\right)$
2	a	(z, z, z) $\left(z + \frac{1}{2}, z + \frac{1}{2}, z + \frac{1}{2}\right)$

VII. SUMMARY AND CONCLUSIONS

Lithium boracites are high-symmetry materials with intriguing properties from both theoretical and technological perspectives. In this work, we show how group theory analysis explains many of the properties of both $Li_4B_7O_{12}Cl$ and $Li_5B_7O_{12.5}Cl$. Detailed first-principles simulations are able to provide a more complete picture of structural, stability, and ionic conductivity properties, consistent with recent experimental evidence [12,15] that $Li_4B_7O_{12}Cl$ and related materials are technologically promising as stable electrolytes for all-solid-state batteries with good Li ion conductivity.

These materials are characterized by a boron oxide framework consisting of tetragonal BO_4 and triangular BO_3 components forming a regular void structure containing Li and Cl ions. The reference space group symmetry [1] of these materials is the face-centered cubic structure $F\bar{4}3c$ (no. 219) which was identified as the high-temperature phase γ-$Li_4B_7O_{12}Cl$ by Jeitschko and coworkers [8]. From those experimental results at lower temperature, which found $32e$ sites to be 25% occupied by Li ions, our first-principles optimization studies found the ground-state structure to be face-centered rhombohedral, having the space group $R3c$ (no. 161), with the rhombohedral angle very close to the cubic angle. Interestingly, the space group $R3c$ is a subgroup of the space group $F\bar{4}3c$ and the relationships between the Wyckoff labels of the two space groups are given in Table VIII. Even more interestingly, the group theory analysis shows how the Li ions which occupy 25% of the $32e$ sites at low temperature are associated with eight sites with Wyckoff label a in the conventional cell of the $R3c$ structure, while the unoccupied 75% are associated with 24 sites with Wyckoff label b in the conventional cell of the $R3c$ structure. In this case, the energetic splitting of the site symmetry is computed to be very small, close to, or within the computational error of the density functional calculations themselves. While group theory analysis predicts the natural interstitial structure of $Li_4B_7O_{12}Cl$, first principles nudged elastic band and molecular dynamics simulations are needed to study the Li ion conductivity properties of this material. Both of these simulation studies show that the natural interstitial sites are occupied at higher temperatures and that the process involves a concerted motion of Li ions at two neighboring sites. While the molecular dynamics simulations are performed at quite high temperatures in order to generate results with significant statistics, the quantitative results assuming $H_r = 1$, are in reasonable agreement

TABLE VII. Wyckoff labels with multiplicity "Mul." and their fractional coordinates for group $F\bar{4}3c$ (no. 219). In this case, the listed fractional coordinates refers to the primitive lattice (x_p, y_p, z_p) expressed in terms of a general point (x, y, z) of the conventional lattice.

Mul.	**Label**	**Fractional coordinates**
24	h	$(x + y - z, -x + y + z, x - y + z)$ $(z + x - y, -z + x + y, z - x + y)$ $(y + z - x, -y + z + x, y - z + x)$ $\left(z + y - x + \frac{1}{2}, -z + y + x + \frac{1}{2}, z - y + x + \frac{1}{2}\right)$ $\left(y + x - z + \frac{1}{2}, -y + x + z + \frac{1}{2}, y - x + z + \frac{1}{2}\right)$ $\left(x + z - y + \frac{1}{2}, -x + z + y + \frac{1}{2}, x - z + y + \frac{1}{2}\right)$ $(-x - y - z, x - y + z, -x + y + z)$ $(z - x + y, -z - x - y, z + x - y)$ $(-y + z + x, y + z - x, -y - z - x)$ $\left(z - y + x + \frac{1}{2}, -z - y - x + \frac{1}{2}, z + y - x + \frac{1}{2}\right)$ $\left(-y - x - z + \frac{1}{2}, y - x + z + \frac{1}{2}, -y + x + z + \frac{1}{2}\right)$ $\left(-x + z + y + \frac{1}{2}, x + z - y + \frac{1}{2}, -x - z - y + \frac{1}{2}\right)$ $(-x + y + z, x + y - z, x - y - z)$ $(-z - x - y, z - x + y, -z + x + y)$ $(y - z + x, -y - z - x, y + z - x)$ $\left(-z + y + x + \frac{1}{2}, z + y - x + \frac{1}{2}, -z - y - x + \frac{1}{2}\right)$ $\left(y - x + z + \frac{1}{2}, -y - x - z + \frac{1}{2}, y + x - z + \frac{1}{2}\right)$ $\left(-x - z - y + \frac{1}{2}, x - z + y + \frac{1}{2}, -x + z + y + \frac{1}{2}\right)$ $(x - y + z, -x - y - z, x + y - z)$ $(-z + x + y, z + x - y, -z - x - y)$ $(-y - z - x, y - z + x, -y + z + x)$ $\left(-z - y - x + \frac{1}{2}, z - y + x + \frac{1}{2}, -z + y + x + \frac{1}{2}\right)$ $\left(-y + x + z + \frac{1}{2}, y + x - z + \frac{1}{2}, -y - x - z + \frac{1}{2}\right)$ $\left(x - z + y + \frac{1}{2}, -x - z - y + \frac{1}{2}, x + z - y + \frac{1}{2}\right)$
12	g	$\left(x, x, -x + \frac{1}{2}\right)$ $\left(x, -x + \frac{1}{2}, x\right)$ $\left(-x + \frac{1}{2}, x, x\right)$ $\left(x + \frac{1}{2}, x + \frac{1}{2}, -x\right)$ $\left(x + \frac{1}{2}, -x, x + \frac{1}{2}\right)$ $\left(-x, x + \frac{1}{2}, x + \frac{1}{2}\right)$ $\left(-x, -x, x + \frac{1}{2}\right)$ $\left(-x, x + \frac{1}{2}, -x\right)$ $\left(x + \frac{1}{2}, -x, -x\right)$ $\left(-x + \frac{1}{2}, -x + \frac{1}{2}, x\right)$ $\left(-x + \frac{1}{2}, x, -x + \frac{1}{2}\right)$ $\left(x, -x + \frac{1}{2}, -x + \frac{1}{2}\right)$
12	f	$(x, x, -x)$ $(x, -x, x)$ $(-x, x, x)$ $\left(x + \frac{1}{2}, x + \frac{1}{2}, -x + \frac{1}{2}\right)$ $\left(x + \frac{1}{2}, -x + \frac{1}{2}, x + \frac{1}{2}\right)$ $\left(-x + \frac{1}{2}, x + \frac{1}{2}, x + \frac{1}{2}\right)$ $(-x, -x, x)$ $(-x, x, -x)$ $(x, -x, -x)$ $\left(-x + \frac{1}{2}, -x + \frac{1}{2}, x + \frac{1}{2}\right)$ $\left(-x + \frac{1}{2}, x + \frac{1}{2}, -x + \frac{1}{2}\right)$ $\left(x + \frac{1}{2}, -x + \frac{1}{2}, -x + \frac{1}{2}\right)$
8	e	(x, x, x) $\left(x + \frac{1}{2}, x + \frac{1}{2}, x + \frac{1}{2}\right)$ $(-3x, x, x)$ $\left(-3x + \frac{1}{2}, x + \frac{1}{2}, x + \frac{1}{2}\right)$ $(x, -3x, x)$ $\left(x + \frac{1}{2}, -3x + \frac{1}{2}, x + \frac{1}{2}\right)$ $(x, x, -3x)$ $\left(x + \frac{1}{2}, x + \frac{1}{2}, -3x + \frac{1}{2}\right)$
6	d	$\left(\frac{1}{4}, \frac{3}{4}, \frac{1}{4}\right)$ $\left(\frac{3}{4}, \frac{1}{4}, \frac{3}{4}\right)$ $\left(\frac{3}{4}, \frac{1}{4}, \frac{1}{4}\right)$ $\left(\frac{1}{4}, \frac{3}{4}, \frac{3}{4}\right)$ $\left(\frac{1}{4}, \frac{1}{4}, \frac{3}{4}\right)$ $\left(\frac{3}{4}, \frac{3}{4}, \frac{1}{4}\right)$
6	c	$\left(\frac{1}{2}, 0, 0\right)$ $\left(0, \frac{1}{2}, 0\right)$ $\left(0, 0, \frac{1}{2}\right)$ $\left(\frac{1}{2}, \frac{1}{2}, 0\right)$ $\left(0, \frac{1}{2}, \frac{1}{2}\right)$ $\left(\frac{1}{2}, 0, \frac{1}{2}\right)$
2	b	$\left(\frac{1}{4}, \frac{1}{4}, \frac{1}{4}\right)$ $\left(\frac{3}{4}, \frac{3}{4}, \frac{3}{4}\right)$
2	a	$(0, 0, 0)$ $\left(\frac{1}{2}, \frac{1}{2}, \frac{1}{2}\right)$

TABLE VIII. Mapping between the multiplicities and Wyckoff labels between the $F\bar{4}3c$ and $R3c$ space groups.

$F\bar{4}3c$	$R3c$
$24h$	$4 \times 6b$
$12g$	$2 \times 6b$
$12f$	$2 \times 6b$
$8e$	$2a + 6b$
$6d$	$6b$
$6c$	$6b$
$2b$	$2a$
$2a$	$2a$

with experimental measurements as shown in Fig. 13. The molecular dynamics results were also analyzed in terms the site occupancies of the host and interstitial Li ion lattice sites according to Eqs. (14) and (15), showing qualitative agreement with experiment.

For analyzing $Li_5B_7O_{12.5}Cl$, group theory analysis also plays an important role in explaining its properties as a very poor ionic conductor. In this case, only one crystal structure has been reported [16] with the face-centered cubic space group $F23$ (no. 196), and this is consistent with the computational results. Interestingly, the $F23$ space group is also a subgroup of the $F\bar{4}3c$ structure and the relationships between the Wyckoff labels of the two space groups is given in Table III. In this case, the $F23$ space group analyzed in the conventional cell has 48 basic elements while the $F\bar{4}3c$ has 96 basic elements. This means that some of the Wyckoff multiplicies and labels of the $F\bar{4}3c$ structure are split into two Wyckoff multiplicies and labels in the $F23$ structure. Additionally, $Li_5B_7O_{12.5}Cl$ contains four extra Li_2O units per conventional cell compared with $Li_4B_7O_{12}Cl$. Comparing the structural diagrams of $Li_4B_7O_{12}Cl$ in Fig. 4(b) and $Li_5B_7O_{12.5}Cl$ in Fig. 5(b), we see evidence of the lower symmetry of the $F23$ structure compared with that of the $F\bar{4}3c$. For $Li_5B_7O_{12.5}Cl$, we see that there are 16 natural interstitial sites in the conventional unit cell. Unfortunately, close examination finds that the placement and energetics associated with these interstitial sites does not result in Li ion migration. Further study using first-principles nudged elastic band and molecular dynamics simulations confirm the conclusion that $Li_5B_7O_{12.5}Cl$ has very poor Li ion conductivity, a result which is consistent with experiment.

Analysis of the phonon spectra in Sec. IV shows that these Li boracites are dynamically stable and analysis of the convex hull based on Li_2O, B_2O_3, and LiCl building blocks in Sec. V show that they are chemically stable as well.

As an extended study of the Li boracite systems, our preliminary simulations suggest that the Li ion conductivity can be enhanced by ionic substitutions to form analog compounds such as $Li_4Al_3B_4O_{12}Cl$, $Li_4B_7S_{12}Cl$, and $Li_4Al_3B_4S_{12}Cl$. In the near future, we plan to investigate the properties of those related materials in more detail.

TABLE IX. Computed energy differences according to Eq. (13) for reactions indicated by the first column. All energy values in eV units, corresponding to those on the convex hull shown in Fig. 8, are evaluated from the static lattice analysis.

Reaction: $R \rightarrow P$	ΔU_{SL}
$Li_5B_7O_{12.5}Cl \rightarrow 2\,Li_2O$[a] $+ 7/2\,B_2O_3$[b] $+$ LiCl[c]	−4.56
$Li_4B_7O_{12}Cl \rightarrow 3/2\,Li_2O + 7/2\,B_2O_3 + LiCl$	−3.53
$LiBO_2$[d] $\rightarrow 1/2\,Li_2O + 1/2\,B_2O_3$	−0.93
$Li_2B_4O_7$[e] $\rightarrow Li_2O + 2\,B_2O_3$	−2.12
Li_3BO_3[f] $\rightarrow 3/2\,Li_2O + 1/2\,B_2O_3$	−1.51
$Li_3B_7O_{12}$[g] $\rightarrow 3/2\,Li_2O + 7/2\,B_2O_3$	−3.36
$Li_6B_4O_9$[h] $\rightarrow 3\,Li_2O + 2\,B_2O_3$	−3.73

[a] Cubic with space group $Fm\bar{3}m$ (no. 225); from Ref. [41].
[b] Orthorhombic with space group $Cmc2_1$ (no. 36); from Ref. [51].
[c] Cubic with space group $Fm\bar{3}m$ (no. 225).
[d] Tetragonal (γ-$LiBO_2$) with space group $I\bar{4}2d$ (no. 122); from Ref. [52].
[e] Tetragonal with space group $I4_1cd$ (no. 110); from Ref. [53].
[f] Monoclinic with space group $P2_1/c$ (no. 14); from Ref. [54].
[g] Triclinic with space group $P\bar{1}$ (no. 2); from Ref. [55].
[h] Monoclinic with space group $P2_1/c$ (no. 14); from Ref. [56].

ACKNOWLEDGMENTS

This work was supported by NSF Grant No. DMR-1940324. Computations were performed on the Wake Forest University DEAC cluster, a centrally managed resource with support provided in part by the University. Helpful discussions with Dr. Zachary Hood (Argonne National Laboratory) and computer assistance from Dr. Sean Anderson (DEAC Cluster administrator, Wake Forest University) are gratefully acknowledged.

APPENDIX A: DETAILS OF THE RELATIONSHIP BETWEEN THE *R3c* AND *F$\bar{4}$3c* SPACE GROUP

It is most convenient to compare the structures using the primitive cell settings. The Wyckoff positions for the $R3c$ (no. 161) system is given in Table VI based on the rhombohedral structure.

The Wyckoff positions for the $F\bar{4}3c$ (no. 219) system is given in Table VII based on the primitive cell of the face-centered cubic structure.

Note that since the $R3c$ and $F\bar{4}3c$ space groups do not have a center of inversion, the set of fractional coordinates $\{(x, y, z)\}$ and the set $\{(-x, -y, -z)\}$ describe equivalent but not identical crystals.

From the results of Tables VII and VI, it is possible to map the relationships between the Wyckoff labels of the $F\bar{4}3c$ and $R3c$ space groups as listed in Table VIII.

APPENDIX B: DETAILS OF THE CONVEX HULL ANALYSIS

In this Appendix, the energy differences from Eq. (13), used to make the convex hull diagram in Fig. 8 are listed in Table IX.

[1] M. I. Aroyo, J. M. Perez-Mato, D. Orobengoa, E. Tasci, G. De La Flor, and A. Kirov, Bulgarian Chem. Commun. **43**, 183 (2011); M. I. Aroyo, J. M. Perez-Mato, C. Capillas, E. Kroumova, S. Ivantchev, G. Madariaga, A. Kirov, and H. Wondratschek, Z. Krist. **221**, 15 (2006); M. I. Aroyo, A. Kirov, C. Capillas, J. M. Perez-Mato, and H. Wondratschek, Acta Cryst. **A62**, 115 (2006).

[2] S. Sueno, J. R. Clark, J. J. Papike, and J. A. Konnert, Am. Mineral. **58**, 691 (1973).

[3] A. Levasseur, C. Fouassier, and P. Hagenmuller, Mater. Res. Bull. **6**, 15 (1971).

[4] M. A. Levasseur and D. J. Lloyd, J. Solid State Chem. **8**, 318 (1973).

[5] J.-M. Réau, A. Levasseur, G. Magniez, and B. Calès, Mater. Res. Bull. **11**, 1087 (1976).

[6] B. Calès, A. Levasseur, C. Fouassier, J. M. Réau, and P. Hagenmuller, Solid State Commun. **24**, 323 (1977).

[7] W. Jeitschko and T. A. Bither, Z. Naturforsch. B **27b**, 1423 (1972).

[8] W. Jeitschko, T. A. Bither, and P. E. Bierstedt, Acta Crystallogr. Sect. B **33**, 2767 (1977); detailed crystal parameters associated with this work are available as cif files from various crystallography databases.

[9] K. Byrappa, K. V. K. Shekar, and R. Rodriguez-Clemente, J. Mater. Res. **8**, 2319 (1993).

[10] T. Nagase, K. Sakane, and H. Wada, J. Sol-Gel Sci. Technol. **13**, 223 (1998).

[11] Y. Ikeda, T. Hiraoka, and S. Ohta, Solid State Ionics **175**, 261 (2004).

[12] D. Tan, F. Wang, T. Pietsch, M. A. Grasser, T. Doert, and M. Ruck, ACS Appl. Energy Mater. **2**, 5140 (2019).

[13] N. I. Sorokin, Phys. Solid State **57**, 314 (2015).

[14] K. Kajihara, N. Tezuka, M. Shoji, J. Wakasugi, H. Munakata, and K. Kanamura, Bull. Chem. Soc. Jpn. **90**, 1279 (2017).

[15] M. Saito, H. Arima, M. Shoji, Y. Kizuki, H. Munakata, K. Kanamura, and K. Kajihara, J. Electrochem. Soc. **168**, 040524 (2021).

[16] M. Vlasse, A. Levasseur, and P. Hagenmuller, Solid State Ionics **2**, 33 (1981).

[17] N. Tezuka, Y. Okawa, K. Kajihara, and K. Kanamura, J. Ceram. Soc. Jpn. **125**, 348 (2017).

[18] P. Hohenberg and W. Kohn, Phys. Rev. **136**, B864 (1964).

[19] W. Kohn and L. J. Sham, Phys. Rev. **140**, A1133 (1965).

[20] P. Giannozzi, S. de Gironcoli, P. Pavone, and S. Baroni, Phys. Rev. B **43**, 7231 (1991).

[21] X. Gonze, Phys. Rev. B **55**, 10337 (1997).

[22] X. Gonze and C. Lee, Phys. Rev. B **55**, 10355 (1997).

[23] S. Baroni, S. De Gironcoli, A. Dal Corso, and P. Giannozzi, Rev. Mod. Phys. **73**, 515 (2001).

[24] P. Giannozzi and S. Baroni, in *Handbook of Materials Modeling*, edited by S. Yip (Springer, Berlin, 2005), pp. 195–214.

[25] P. E. Blöchl, Phys. Rev. B **50**, 17953 (1994).

[26] J. P. Perdew, A. Ruzsinszky, G. I. Csonka, O. A. Vydrov, G. E. Scuseria, L. A. Constantin, X. Zhou, and K. Burke, Phys. Rev. Lett. **100**, 136406 (2008).

[27] N. A. W. Holzwarth, A. R. Tackett, and G. E. Matthews, Comput. Phys. Commun. **135**, 329 (2001); available from the website, http://pwpaw.wfu.edu.

[28] X. Gonze, F. Jollet, F. A. Araujo, D. Adams, B. Amadon, T. Applencourt, C. Audouze, J.-M. Beuken, J. Bieder, A. Bokhanchuk, E. Bousquet, F. Bruneval, D. Caliste, M. Côté, F. Dahm, F. D. Pieve, M. Delaveau, M. Di Gennaro, B. Dorado, C. Espejo *et al.*, Comput. Phys. Commun. **205**, 106 (2016); available at the website, https://www.abinit.org.

[29] X. Gonze, B. Amadon, G. Antonius, F. Arnardi, L. Baguet, J.-M. Beuken, J. Bieder, F. Bottin, J. Bouchet, E. Bousquet, N. Brouwer, F. Bruneval, G. Brunin. T. Cavignac, J.-B. Charraud, W. Chen, M. Côté, S. Cottenier, J. Denier, G. Geneste *et al.*, Comput. Phys. Commun. **248**, 107042 (2020); available from the website, https://www.abinit.org/.

[30] P. Giannozzi, O. Andreussi, T. Brumme, O. Bunau, M. B. Nardelli, M. Calandra, R. Car, C. Cavazzoni, D. Ceresoli, M. Cococcioni, N. Colonna, I. Carnimeo, A. D. Corso, S. de Gironcoli, P. Delugas, R. A. DiStasio Jr., A. Ferretti, A. Floris, G. Fratesi, G. Fugallo *et al.*, J. Phys.: Condens. Matter **29**, 465901 (2017); available from the website, http://www.quantum-espresso.org.

[31] P. Giannozzi, O. Baseggio, P. Bonfà, D. Brunato, R. Car, I. Carnimeo, C. Cavazzoni, S. de Gironcoli, P. Delugas, F. F. Ruffino, A. Ferretti, N. Marzari, I. Timrov, A. Urru, and S. Baroni, J. Chem. Phys. **152**, 154105 (2020).

[32] A. Kokalj, Comput. Mater. Sci. **28**, 155 (2003); code available at the website, http://www.xcrysden.org.

[33] K. Momma and F. Izumi, Appl. Crystallogr. **44**, 1272 (2011); code available from the website, http://jp-minerals.org/vesta/en/.

[34] H. T. Stokes and D. M. Hatch, J. Appl. Crystallogr. **38**, 237 (2008); available from the website, https://stokes.byu.edu/iso/findsym.php.

[35] C. F. Macrae, I. Sovago, S. J. Cottrell, P. T. A. Galek, P. McCabe, E. Pidcock, M. Platings, G. P. Shields, J. S. Stevens, M. Towler, and P. A. Wood, J. Appl. Crystallogr. **53**, 226 (2020).

[36] We note that the lattice constants and rhombohedral angles found in our optimization studies are slightly dependent on initial configuration and also the results differ slightly in the QUANTUM ESPRESSO and ABINIT codes. We believe that these differences are due to the shallow nature of the potential energy surface of this system near equilibrium. However, the reported results are expected to be reliable within the expected overall error of calculations of this type of ±0.001 eV per formula unit.

[37] For example, in the conventional cell setting of the $F23$ structure, it is possible to generate a $F\bar{4}3c$ structure by placing identical atoms at $48h$ sites generated with coordinates (x, y, z) and an additional $48h$ sites generated with coordinates $(y + \frac{1}{2}, x + \frac{1}{2}, z + \frac{1}{2})$.

[38] Y. Hinuma, G. Pizzi, Y. Kumagai, F. Oba, and I. Tanaka, Comput. Mater. Sci. **128**, 140 (2017).

[39] Y. Li, Z. D. Hood, and N. A. W. Holzwarth, Phys. Rev. Materials **4**, 045406 (2020).

[40] Y. Li, Z. D. Hood, and N. A. W. Holzwarth, Phys. Rev. Materials **5**, 085403 (2021).

[41] T. W. D. Farley, W. Hayes, S. Hull, M. T. Hutchings, and M. Vrtis, J. Phys.: Condens. Mat. **3**, 4761 (1991).

[42] D. D. Lee, J. H. Choy, and J. K. Lee, J. Phase Equilib. **13**, 365 (1992).

[43] S. P. Ong, L. Wang, B. Kang, and G. Ceder, Chem. Mater. **20**, 1798 (2008).

[44] H. Jónsson, G. Mills, and K. W. Jacobsen, in *Classical and Quantum Dynamics in Condensed Phase Simulations*, edited

by B. J. Berne, G. Ciccotti, and D. F. Coker (World Scientific, Singapore, 1998), pp. 385–404.

[45] G. Henkelman, B. P. Uberuaga, and H. Jónsson, J. Chem. Phys. **113**, 9901 (2000).

[46] G. Henkelman and H. Jónsson, J. Chem. Phys. **113**, 9978 (2000).

[47] Here we are using the Wyckoff labels for the $F23$ space group as described in Table III.

[48] Y. Haven and B. Verkerk, Phys. Chem. Glasses **6**, 38 (1965).

[49] Y. Li, Z. D. Hood, and N. A. W. Holzwarth, Phys. Rev. Materials **5**, 085402 (2021).

[50] Z. Zhang, P.-N. Roy, H. Li, M. Avdeev, and L. F. Nazar, J. Am. Chem. Soc. **141**, 19360 (2019).

[51] C. T. Prewitt and R. D. Shannon, Acta Crystallogr. Sect. B **24**, 869 (1968).

[52] M. Marezio and J. P. Remeika, J. Chem. Phys. **44**, 3348 (1966).

[53] J. Krogh-Moe, Acta Crystallogr. **15**, 190 (1962).

[54] V. F. Stewner, Acta Crystallogr. Sect. B **27**, 904 (1971).

[55] A. Jiang, S. Lei, Q. Huang, T. Chen, and D. Ke, Acta Crystallogr. Sect. C **46**, 1999 (1990).

[56] G. Rousse, B. Baptiste, and G. Lelong, Inorg. Chem. **53**, 6034 (2014).